Environmental Science Nano

ROYAL SOCIETY OF CHEMISTRY

PAPER

View Article Online
View Journal | View Issue

Cite this: *Environ. Sci.: Nano*, 2022, **9**, 3859

Multi-method approach for analysis of road dust particles: elemental ratios, SP-ICP-TOF-MS, and TEM†

Feiyun Tou,[a] Md. Mahmudun Nabi,[b] Jingjing Wang,[b] Mahdi Erfani,[c] Erfan Goharian,[c] Jing Chen,[d] Yi Yang *[a] and Mohammed Baalousha *[b]

Road dust particles including nanoparticles (NPs), with heterogeneous composition, are significant carriers of metals/metalloids and can be further transported into the atmosphere or surface runoff. However, their elemental composition remains poorly defined. In this study, seven road dust samples were collected from different areas in Shanghai, China and were analyzed for total metal concentrations, particle elemental composition and ratios, morphology, composition, and crystalline phases. Overall, the road dust particles were characterized by high concentrations of Fe, Ti, Al, Cr, Ci, V Ni, Cu, Zn, Sn, and Sb, which varied among the samples. Four potential sources of metals were identified using PCA analysis including natural sources, exhaust and non-exhaust emissions, and vehicle electronics. The bulk elemental ratios of Ti/Nb, Ti/Al, Ti/Fe, Pb/Nb, Sn/Nb and W/Nb in the road dust samples were higher than the corresponding reference ratios indicating that the road dust was contaminated with Ti, Pb, Sn, and W. Anthropogenic Ti, Pb, Sn and W were estimated by mass balance calculation and varied between 0.25 and 1.48 × 10^6 μg kg^{-1}, 0.19 and 1.21 × 10^5 μg kg^{-1}, 0.98 and 4.22 × 10^4 μg kg^{-1}, and 0.12 and 1.01 × 10^4 μg kg^{-1}, respectively. The number concentration of NPs was determined by SP-ICP-TOF-MS and was 0.66–3.3 × 10^{10} particles per g for Ti-containing NPs, 0.23–1.51 × 10^{10} particles per g for Pb-containing NPs, 0.28–3.10 × 10^9 particles per g for Sn-containing NPs, and 1.34–9.38 × 10^8 particles per g for W-containing NPs, respectively. TEM analysis further confirmed the occurrence of both natural and anthropogenic Ti- and W-containing NPs and the contamination of Pb- and Sn-containing NPs in Shanghai road dust. These NPs could originate from the non-exhaust emission of vehicles and coal combustion. Overall, this study provides a reliable comprehensive approach for the characterization of road dust particles and new insights into the nature of Ti-, Pb-, Sn-, and W-containing particles in dust samples.

Received 28th April 2022,
Accepted 23rd August 2022

DOI: 10.1039/d2en00409g

rsc.li/es-nano

Environmental significance

The identification, discrimination and quantification of anthropogenic and natural metal-containing nanoparticles (NPs) in the environment are essential to understand the occurrence, fate, behavior and environmental risks of these NPs. In the present study, by combining elemental analysis, SP-ICP-TOF-MS analysis and microscopy analysis, hundreds of millions to tens of billions of Ti-, Pb-, Sn-, and W-containing NPs were detected in road dust in Shanghai, and the concentrations of anthropogenic Ti-, Pb-, Sn-, and W were estimated. These NPs could originate from the non-exhaust emission of vehicles and coal combustion, and enter the atmosphere and water environment by resuspension and runoff, posing potential risks to human health and aquatic organisms.

[a] *Key Laboratory of Geographic Information Science (Ministry of Education), School of Geographical Sciences, East China Normal University, 500 Dongchuan Road, Shanghai 200241, China. E-mail: yyang@geo.ecnu.edu.cn; Tel: +86 21 54341196*

[b] *Center for Environmental Nanoscience and Risk, Department of Environmental Health Sciences, Arnold School of Public Health, University of South Carolina, Columbia, South Carolina, 29201, USA. E-mail: mbaalous@mailbox.sc.edu; Tel: +1 803 777 7177*

[c] *Department of Civil and Environmental Engineering, University of South Carolina, SC 29208, USA*

[d] *State Key Laboratory of Estuarine and Coastal Research, Yangtze Delta Estuarine Wetland Ecosystem Observation and Research Station, Ministry of Education & Shanghai, East China Normal University, 3663 North Zhongshan Road, Shanghai 200062, China*

† Electronic supplementary information (ESI) available. See DOI: https://doi.org/10.1039/d2en00409g

1. Introduction

Air pollution is one of the most important and concerning global environmental issues. Recent studies demonstrated that outdoor air pollution, mostly by fine and inhalable particles with an aerodynamic diameter smaller than 2.5 μm ($PM_{2.5}$), has been estimated to lead to 4.14 million premature deaths per year worldwide and contributed to 1.42 million deaths in China.[1–3] Moreover, airborne ultrafine particles, which are smaller than 100 nm, can even penetrate the alveolar area of the lungs and transfer through the bloodstream to other organs, including the heart and brain.[4–6] With the rapid development of urbanization, an increasing number of natural surfaces (soils, rocks, vegetation, natural surface water) have dramatically shifted to impervious surfaces (buildings, roads, parking lots, sidewalks, *etc.*).[7] Road dust consists of solid particles that are generated by any mechanical processing of materials, including crushing, grinding, rapid impact, handling, detonation, and decrepitation of organic and inorganic materials such as rock, ore, and metal.[8] It can be resuspended into the air as a contributor of $PM_{2.5}$ and transported to nearby surface water by urban runoff with significant quantities of contaminants (such as toxic metals and organic pollutants), increasing threats to the environment and human health.[9,10]

It is a great challenge to directly quantify metal-containing particles in complex environmental samples and further differentiate natural from anthropogenic particles. Electron microscopy (EM) techniques, such as scanning transmission electron microscopy (STEM) and scanning electron microscopy (SEM), coupled with accessory capabilities such as energy dispersive X-ray spectroscopy (EDS) and selected area electron diffraction (SAED), have been recognized by the scientific community as powerful tools to provide detailed information including particle size, morphology, chemical composition, and crystal structure on a single-particle basis.[7,11,12] Although EM techniques can differentiate naturally occurring from anthropogenic particles in some cases,[7,11] they cannot provide quantitative abundance or concentration information. Single particle inductively coupled plasma time-of-flight mass spectrometry (SP-ICP-TOF-MS) is a unique and promising approach that enables multi-element detection and quantification of various metal and metal-containing particles, providing multidimensional information including multi-element composition, size/mass distribution, and number concentration, and it is the only ICP-MS-based method that allows for quantitative untargeted multi-element measurements from individual particles and could enable differentiating natural from anthropogenic particles.[13–16] At present, it has been used to identify and quantify engineered and natural nanoparticles in soils,[13,17,18] surface/rain waters,[14,18–20] and effluents from wastewater treatment plants.[15]

Shanghai, with an area of 6340 km^2 and a population of more than 24 million, is a sprawling megacity in China. With increasing population, motorization, urbanization and industrial activities, Shanghai is under serious stress from airborne contaminants, including airborne particles. In the present study, seven road dust samples were collected from different areas in Shanghai and were characterized with a series of techniques, including inductively coupled plasma-mass spectrometry (ICP-MS), SP-ICP-TOF-MS, SEM, and TEM coupled with EDS and SAED. The overall aim of this study was to characterize road dust using a multi-method analytical approach in order to better understand the nature of particles in road dust and to develop approaches to differentiate natural from anthropogenic particles and to quantify their concentrations. The specific objectives of this study are (1) to realize the source apportionment of metals in dust samples based on the principal component analysis (PCA), (2) to differentiate the natural particles from the anthropogenic particles and quantify their concentrations, (3) to determine the elemental composition of multi-metal bearing particles at the single particle level, and (4) to identify the dominant metal-containing NPs based on electron microscopy techniques. The information generated in this study will provide a comprehensive approach for the characterization of road dust particles and give new insights into the nature of metal-containing particles in Shanghai, China.

2. Materials and methods

2.1. Sample collection and preparation

Seven road dust samples were collected from the road surface in various functional areas in Shanghai. The distribution and the corresponding detailed information of the seven road dust samples, *i.e.* SJP, JIA, WU, ZSTP, LT, JHSRS, and ECNU, are shown in Fig. 1 and Table 1, respectively. For each road dust sample, around 30 g of dust was swept from each side of the pavement, along 100 m, using a plastic brush and tray, and then mixed thoroughly to obtain a homogeneous sample.

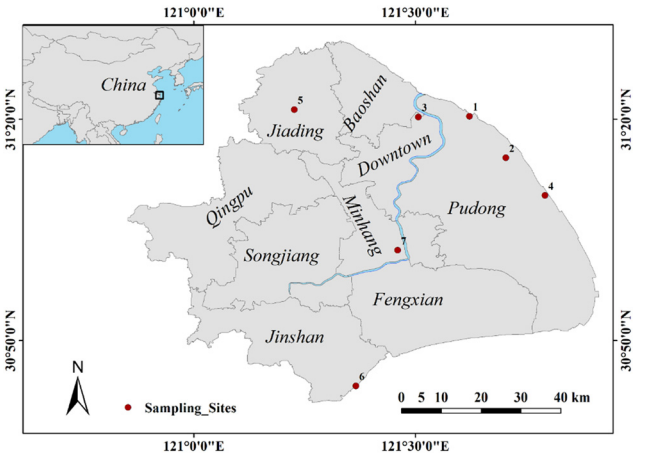

Fig. 1 Distribution of sampling sites.

Table 1 Description of sampling sites

	Sampling site	Location/District	Latitude (°N)	Longitude (°E)	Site ambient environment
1	**San Jia port**	**Pudong**	**31°22′08″**	**121°30′12″**	**Near a large-scale sand mining ship factory**
2	Jinqiao Industrial Area	Pudong	31°14′52″	121°36′23″	In a manufacturing industrial park
3	Wujiaochang	Yangpu	31°18′18″	121°30′37″	In a densely populated and busy car commercial district
4	Zhangjiang Science and Technology park	Pudong	31°14′45″	121°42′15″	In a high-tech industrial park
5	Luojing town	Baoshan	31°28′17″	121°19′25″	Heavy traffic density road, near the exit of a highway toll station
6	**Jinshan high speed rail station**	**Jinshan**	**30°43′50″**	**121°21′57″**	**Near a high-speed rail train station**
7	East China Normal University	Minhang	31°2′14″	121°27′36″	In a university campus

Note: samples analyzed by TEM were highlighted in bold. These samples were selected due to the high concentrations of suspected particulate contamination in these two sites.

All the samples were passed through a 48 mesh sieve to remove large particles, debris and fibers, and then stored in valve bags in the dark at room temperature.

Twenty milligrams of the road dust samples were mixed with 30 mL ultrapure water (UPW, PURELAB Option-Q, ELGA, Buckinghamshire, UK) in 50 mL acid-washed polypropylene centrifuge tubes and overhead rotated on a tube rotator (Fisher Scientific, Shanghai, China) at 40 rpm overnight. The well-dispersed mixture was bath sonicated (Branson 2800, 40 kHz, Eppendorf, Hamburg, Germany) for 2 h to disrupt dust microaggregates and enhance the release dispersion of natural particles.[21] A 1 μm size fraction was then separated by centrifugation (Eppendorf, 5810 R, Germany) at 775*g* for 5 min based on a particle density of 2.5 g cm^{-3} and Stokes' law calculation,[22] and the top 20 ml of the supernatant was transferred into 50 mL acid-washed polypropylene centrifuge tubes and stored at 4 °C before any further analysis. The collected fractions were diluted 5000-fold in UPW and sonicated for 15 min in a bath sonicator prior to SP-ICP-TOF-MS analysis.

2.2. Elemental analysis

The road dust samples were digested in a custom-made digestion oven in a metal-free HEPA filtered air clean lab. To avoid possible contamination, the digestion oven has a Teflon-covered hotplate secured in a plastic box equipped with double-HEPA filtered forced air. 0.2 g of dust was weighed (Mettler Toledo) and transferred into a 15 mL Teflon digestion vessel (Savillex). The samples were treated with 1 mL of 30% H_2O_2 and heated on the hot plate at 70 °C for 2 hours to digest organic matter. H_2O_2 was evaporated after the completion of the reaction. The dried sample was then digested with 2 mL of distilled HF : HNO_3 mixture (3 : 1, ACS grade acids) at 110 °C for 48 hours. The liquid was evaporated at the end of digestion. 1 mL distilled concentrated HNO_3 (~70%) was added to the residue and left to dry at 110 °C. This step was repeated twice to ensure break down of any possible insoluble fluoride salts generated in the digestion process. The residue was dissolved in 5 mL of 1% HNO_3 (TraceMetal grade, Fisher Chemical) and diluted in ultrapure water (UPW, PURELAB Option-Q, ELGA LabWater). The solution was bath sonicated (Branson, Model 2800, 40 kHz) for 10 min and left in the digestion oven at 50 °C for 2 hours. Then the solution was transferred into a 15 mL polypropylene centrifuge tube (10% ACS grade HNO_3 pre-washed, Fisherbrand). Prior to ICP-MS analysis, the samples were centrifuged at 3100*g* for 5 min to remove any undigested minerals, and the supernatant was diluted 1000 times with 1% TraceMetal grade HNO_3.

The elemental concentration of the digested samples was determined using a Perkin Elmer NexION 350D inductively coupled plasma-mass spectrometer. The standard tuning procedure was performed before analysis for instrument maintenance. The isotopes measured were ^{24}Mg, ^{27}Al, ^{45}Sc, ^{49}Ti, ^{51}V, ^{53}Cr, ^{55}Mn, ^{57}Fe, ^{59}Co, ^{60}Ni, ^{65}Cu, ^{66}Zn, ^{69}Ga, ^{72}Ge, ^{85}Rb, ^{88}Sr, ^{89}Y, ^{90}Zr, ^{93}Nb, ^{98}Mo, ^{107}Ag, ^{111}Cd, ^{118}Sn, ^{133}Cs, ^{137}Ba, ^{139}La, ^{140}Ce, ^{141}Pr, ^{142}Nd, ^{152}Sm, ^{153}Eu, ^{158}Gd, ^{159}Tb, ^{164}Dy, ^{165}Ho, ^{166}Er, ^{169}Tm, ^{174}Yb, ^{175}Lu, ^{180}Hf, ^{181}Ta, ^{184}W, and ^{195}Pt, ^{208}Pb, ^{232}Th, and ^{238}U. A dissolved multi-element standard mixture of ICP Complete Group Calibration Standard (BDH Chemicals) and ICP Refractory Element Group Calibration Standard (BDH Chemicals) diluted in 1% (v/v) nitric acid (TraceMetal grade, Fisher Chemical) was used for mass concentration calibration ranging from 0.1 to 1000 μg L^{-1}. ^{115}In was monitored as the internal standard (ICP Internal Element Group Calibration Standard, BDH Chemicals) for quality control. The kinetic energy discrimination (KED) mode (with helium gas flow rates of 0.3–0.45 mL min^{-1}) was used to eliminate the polyatomic interference. The parameters of ICP-MS and SP-ICP-TOF-MS are listed in Table S1.†

2.3. Single particle analysis

Single particle analysis of the diluted dust particle extracts was performed using ICP-TOF-MS (TOFWERK, Thun, Switzerland) to determine all isotopes within a single particle simultaneously.[23] All samples and procedural blanks were analyzed in triplicate and data were collected for 10 minutes for each replicate. The replicates were combined for all following data analyses due to the low detection frequency of some elements. Element specific instrument sensitivities were measured with a multi-element solution mix prepared

from a multi-element solution (0, 1, 2, 5, and 10 μgL^{-1} multi element standard, diluted in 1% HNO_3, BDH Chemicals, Radnor, PA, USA). The transport efficiency was calculated using the known size approach[24] using both Au ENMs with a certified particle size of 60 nm (NIST RM8013 Au, Gaithersburg, MD, USA) prepared in UPW and Au ionic standard solutions (0, 1, 2, 5, and 10 μgL^{-1}, diluted in 1% HCl, BDH Chemicals, West Chester, PA, USA). Using a standard tuning solution, the ICP-TOF-MS mass spectra were calibrated based on $^{18}H_2O^+$, $59Co^+$, $115In^+$, $140Ce^+$, and $^{238}U^+$ target isotopes in TofDaq Viewer (Version, TOFWERK) prior analysis. Particle/baseline signal separation, particle signals, and particle mass were determined from the mass-calibrated ICP-TOF-MS spectra using or in Tofware (Version, TOFWERK). The particle detection threshold was calculated for each isotope according to eqn (1).[25]

$$\text{Threshold} = \text{Mean} + (3.29\sigma + 2.71) \quad (1)$$

Mean and σ are those of background signals in the analysis window of 100 data points. The data for each isotope were treated separately, but the time stamps were kept throughout the data processing for every isotope, allowing for identification of isotope correlations in a single particle.

2.4. Clustering analysis of SP-ICP-TOF-MS data

The detected NPs were classified into single and multiple metal nanoparticles (smNPs and mmNPs). The smNPs were considered as their own clusters because the NP mass and number concentrations are not sufficient to cluster smNPs. The mmNPs were classified into clusters of NPs of similar elemental composition using an unsupervised data analysis approach (agglomerative hierarchical clustering) using MATLAB, to identify clusters/groups of NPs of similar elemental composition and to identify their mean elemental composition, with the aim of identifying anthropogenic NPs in the different dust samples. The mmNPs were processed through a two-stage (*e.g.*, intra- and inter- sample) hierarchical clustering analysis following a method described elsewhere.[17,26] First, intra-sample clustering was performed on all metal masses in each NP to generate clusters that best account for variance in NP metallic composition in each sample. The correlation distance, which represents the dissimilarity of the NP compositions to one another, was used as the distance metric for clustering. A smaller correlation distance indicates that the elemental compositions of two particles are very close to each other and *vice versa*. After the correlation distance between all NPs was calculated, hierarchical clustering was performed using the average correlation distance. This step generated a cluster dendrogram for each sample, which was divided into major clusters using a distance cutoff. The distance cutoff was determined by visually inspecting the dendrogram and through trial and error in order to minimize the variance/diversity in NP elemental composition in the major clusters. A cluster representative was determined for each major cluster as the mean of metal mass in individual NPs within each cluster considering all elements that occurred in at least five percent of NPs within the cluster. For each major cluster, the mass fraction of a given metal in each particle was determined as the mass of that metal divided by the sum of masses of all metals in that NP. Then, the mean cluster composition was determined as the mean of metal mass fraction in all NPs in the cluster. The clusters were labeled by the three elements with the highest mean mass fractions within each cluster. Second, inter-sample clustering was performed on the major cluster representatives identified in the intra-sample clustering to group/cluster the similar NP major clusters identified in the different samples. This step generates a cluster dendrogram for intra-sample cluster representatives, which was divided into major clusters using a distance cutoff as performed for the intra sample clusters. Finally, heat maps were generated by comparing the number of NPs in each major cluster among the different samples. Subsequently, selected elemental ratios were determined on a particle-per-particle basis considering all particles containing the two elements and the elemental ratio distribution was determined. The number concentration (NP g^{-1}) of the total, smNPs, mmNPs, and cluster members were determined according to eqn (2).

$$\text{Number concentration} = \frac{\text{Number of detected NPs} \times \text{dilution factor} \times \text{extraction volume}}{\text{aquisition time} \times \text{liquid flow} \times \text{transport efficiency} \times \text{dust mass}} \quad (2)$$

2.5. Calculation of anthropogenic Ti and W concentrations

The anthropogenic titanium concentration was determined by mass balance calculations based on shifts in elemental concentration ratios of Ti/Nb, Ti/Al, and Ti/Fe in road dust relative to the corresponding elemental ratios in 28 core sediment samples (Tables S2 and S3†) collected in the sampling area for the background level of each element.

$$\text{Ti}_{\text{natural}} = \text{Nb}_{\text{sample}} \times \left(\frac{\text{Ti}}{\text{Nb}}\right)_{\text{reference}} \quad (3)$$

$$\text{Ti}_{\text{anthropogenic}} = \text{Ti}_{\text{sample}} - \text{Ti}_{\text{natural}} \quad (4)$$

where $\text{Ti}_{\text{natural}}$ is the natural Ti concentration in the sample, $\text{Ti}_{\text{sample}}$ is the total Ti concentration measured in each dust sample, and $(\text{Ti/Nb})_{\text{reference}}$ is the average Ti/Nb concentration ratio of the local reference samples, which were generally in close agreement with the average crustal values (Table S3†). $\text{Ti}_{\text{anthropogenic}}$ is the concentration of anthropogenic Ti. Anthropogenic W, Pb, and Sn concentrations were calculated using eqn (3) and (4) by replacing Ti with W, Pb, and Sn and using W/Nb, Pb/Nb, and Sn/Nb ratios, respectively.

2.6. Transmission electron microscopy

Selected samples (SJP and JHSRS) were characterized using scanning and transmission electron microscopy. Each sample was dispersed in Milli-Q water by ultrasonication and then dropped onto a 300 mesh copper TEM grid with a lacey carbon support film (Electron Microscopy Sciences, USA). A scanning electron microscope (SEM, Hitachi S4800, Japan) equipped with an energy dispersive X-ray spectrometer (EDS) system and a transmission electron microscope (TEM, JEOL 2100, Japan) coupled with EDS and selected area electron diffraction (SAED) were applied to characterize the morphology, composition, and diffraction patterns of the NPs.

2.7. Principal component analysis

The principal component analysis (PCA) using SPSS software following the varimax rotation method was applied for the source apportionment of metals in dust samples. PCA is a statistical method of dimension reduction. It can realize the change from multiple variables (indicators) to a few comprehensive variables (indicators) which can reflect most information of the original multiple variables.

3. Results and discussion

3.1. Elemental contamination

Total concentrations of Al, Ti, V, Cr, Fe, Co, Ni, Cu, Zn, Sn, Ce, Zr, Pb and W in dust samples are shown in Fig. S1.† Ti, Fe and Al, with average concentrations of 4.3×10^6, 3.5×10^7, and 3.1×10^7 μg kg^{-1}, respectively, are the most abundant metals in Shanghai road dust, which is 2–4 orders of magnitude higher than all the other metals. Zn followed with an average concentration of 9.2×10^5 μg kg^{-1}. W exhibited the lowest abundance, with an average of 5.2×10^3 μg kg^{-1} in all the dust samples. Noticeably, JHSRS dust collected near a high-speed rail train station exhibited the highest concentrations of Ti, Al, Sn, W, Ce, Zr, and Zn and elevated concentration of Pb. Zn concentrations were also found in the dust collected from JIA, a manufacturing industrial area (Fig. S1†). Dust from SJP, near a large-scale sand mining ship factory, exhibited the highest concentrations of Fe, Co, Cr, V, Ni, Cu, and Pb compared to all the other samples (Fig. S1†). Fe was also elevated in the LT and JHSRS dust samples. These elevated metals indicate the possibility of metal contamination (including metal-containing particles) in the relevant areas.

The principal component analysis (PCA) using SPSS software following the varimax rotation method was applied for the source apportionment of metals in dust samples. As presented in Table S4,† four components were identified. **PC1** had the highest loading of Nd, Tb, Dy, Sm, Al, Gd, Ho, Pr, Tm, Er, Zr, Yb, Hf, Lu, Eu, Nb, Y, Sc, La, Ta, Th, Ce, Ga, Ti, Ag, U and Mg, explaining 51.2% of the variance. Most of these metals are common rare earth elements, so PC1 could be heavily influenced by the soil matrix, dominantly representing the natural source. **PC2** explained 22.3% of the variance and was related to Ni, V, Fe, Co, Ge, Cu, Mn, Sr, Cr, Mo, and Pt. These elements are commonly used catalysts in vehicle exhaust converters,[27–29] indicating that PC2 could represent a source of vehicle exhaust. **PC3** was linked to Sn, Zn, Cd, In, Pb, Ba and W, explaining 14% of the variance. Lead–tin alloy is an important raw material for industrial manufacturing, including automobile manufacturing, and W and Zn are also used in car parts and tires, respectively.[30–33] These metals could be emitted by the friction of the brake pads and other vehicle components, indicating that PC3 could represent the metals from the non-exhaust emission. **PC4** was related to Cs and Rb, explaining 7.4% of the variance. Cs and Rb are important materials for making photocells and vacuum tubes, which could be released from the electronic system of cars. Similar conclusions could be obtained by the correlation analysis. As shown in Table S5,† the metals in each PC group exhibited strong correlations with each other at 0.01 level, indicating the same or similar source. Some metals showed strong correlation with metals in other PC groups. For example, W in PC3 also showed strong correlation with La, Ce, and Ga in PC1, indicating another source (natural source) of W. This result is consistent with the single particle analysis of W-containing particles in section 3.3. In this section, the natural source and anthropogenic source of W were demonstrated in Shanghai road dust. To further confirm the contamination of other metals (such as Ti, Pb, Sn, and W), elemental ratio analysis was implemented.

3.2. Bulk elemental ratios and anthropogenic elemental concentrations

Natural TiO_2 minerals, such as rutile and ilmenite, have been shown to be the dominant carrier (*e.g.*, > 90–95% of the whole rock content) for Ti, Nb, Ta, Sb, and W, as well as an important carrier (*e.g.*, 5–45% of the whole rock content) for V, Cr, Mo, and Sn, such as TiO_2-bearing metamorphic rocks.[34] The bulk elemental ratios of Ti/Nb, Ti/Al, and Ti/Fe were higher than the average reference elemental ratios (*e.g.*, 284 ± 17, 0.07 ± 0.013, and 0.133 ± 0.020, respectively, Table S3†) for all the dust samples except for Ti/Fe in SJP dust (Fig. S2a–c†). These findings suggest that all the samples were contaminated with anthropogenic Ti-containing particles. Although Ti/Nb and Ti/Fe for the LT dust, collected near the exit of a highway toll station, were lower than the corresponding mean reference ratios, they were still within the natural variability range (Fig. S2a–c†). The lower Ti/Fe in the SJP (near a large-scale sand mining ship factory) dust than the natural reference ratio could be attributed to natural variability in the dust elemental composition or to co-contamination of road dust with Fe in this dust sample. The former reason can be ruled out because the Ti/Fe elemental ratios in Ti- and Fe-bearing particles in the SJP dust are typical of natural minerals with an average elemental ratio of 4.7 ± 20.3 (Fig. S3b†). Thus, the lower bulk Ti/Fe elemental

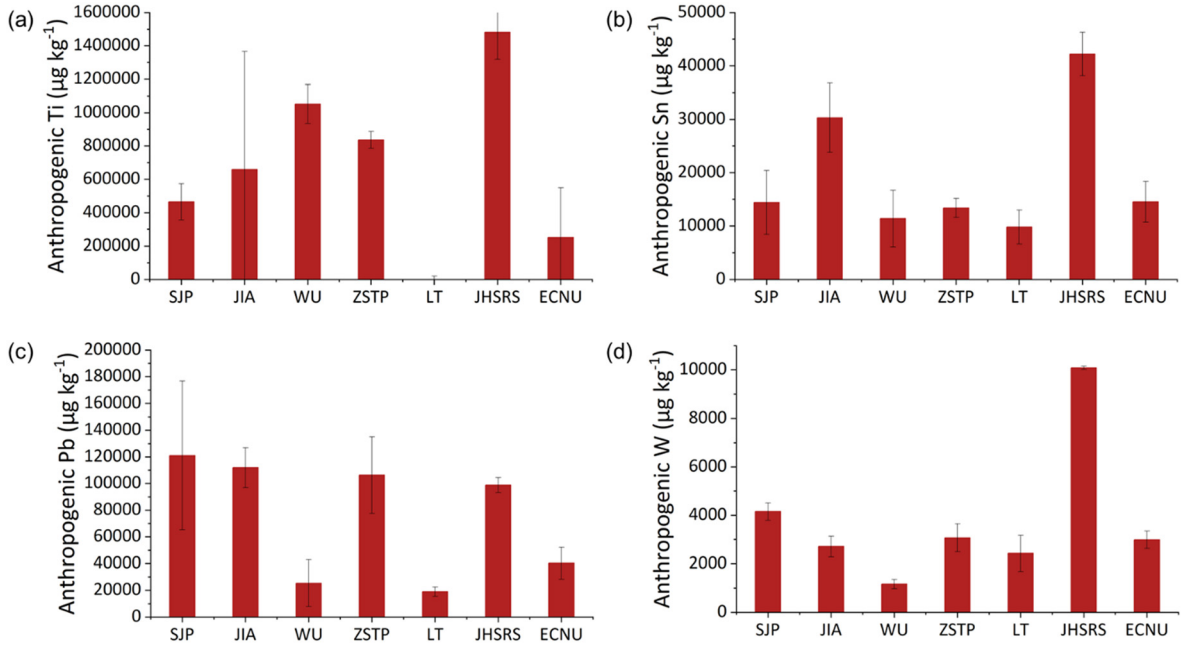

Fig. 2 Estimated anthropogenic (a) Ti, (b) Sn, (c) Pb, and (d) W concentrations using mass balance calculations and shifts in Ti/Nb, W/Nb, Pb/Nb, and Sn/Nb, respectively.

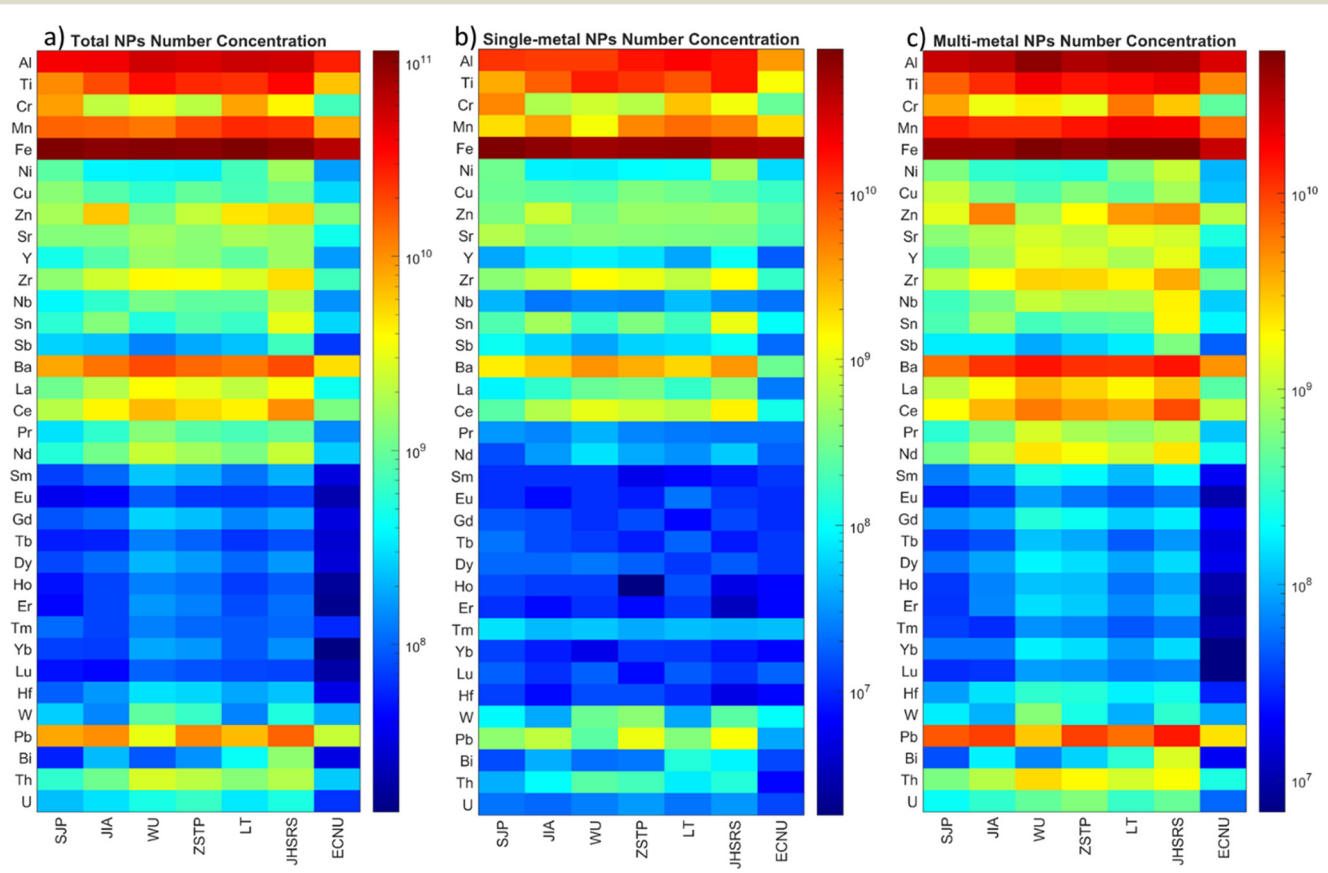

Fig. 3 Heat maps of the number concentration (particles per g) of (a) total number of NPs, (b) single metal NPs (smNPs), and (c) multi-metal NPs (mmNPs) measured by SP-ICP-TOF-MS.

ratio in San Jia Port is due to the co-contamination of the SJP dust with Fe-bearing particles. On the other hand, the elemental ratios of Ti/W were lower than the natural elemental ratios (Fig. S2d†), suggesting that these dust samples were contaminated with W. Given that the dust samples were also contaminated with anthropogenic Ti, the elemental ratios of W/Nb, Pb/Nb, and Sn/Nb were used to identify W, Pb, and Sn contamination (Fig. S2e–g†), where all the dust samples exhibited higher W/Nb, Pb/Nb, and Sn/Nb ratios than the natural reference ratios (0.11 ± 0.01, 1.46 ± 0.22, and 0.21 ± 0.03, respectively, Table S3†), and the average crustal ratios (0.16, 1.42, and 0.18, respectively, Table S3†).

The anthropogenic Ti, W, Pb, and Sn concentrations were estimated by mass balance calculations based on the Ti/Nb, W/Nb, Pb/Nb, and Sn/Nb elemental ratios, respectively, according to eqn (3) and (4) (Fig. 2). The estimated anthropogenic Ti, Pb, Sn and W were 0.25–1.48 × 10^6 μg kg^{-1}, 0.19–1.21 × 10^5 μg kg^{-1}, 0.98–4.22 × 10^4 μg kg^{-1}, and 0.12–1.01 × 10^4 μg kg^{-1}, respectively. Anthropogenic Ti contamination in road dust might be attributed to particle release from painted surfaces, photocatalytic surfaces, and white road marking.[35,36] The JHSRS dust sample collected near a high-speed rail train station displayed the highest anthropogenic W, Pb, and Sn concentrations, which might be attributed to the railway coating material and/or vehicle brake pads.[30,32] We note that the estimated anthropogenic elemental concentrations in this study represent the lower bound of the anthropogenic elemental contamination rather than a precise measure of the anthropogenic fraction concentrations. This is because the estimated anthropogenic concentrations could be underestimated due to the co-contamination of the road dust samples with the reference element (*e.g.*, Nb).

3.3. Multi element analysis on single nanoparticles

In addition to the principal component analysis and the bulk elemental ratio analysis, multi-element single particle analysis was performed to further identify metal containing particle contamination in the road dust samples. The number concentrations of all NPs, single metal NPs (smNPs), and multi-metal NPs (mmNPs) are presented in Fig. 3. Fe (60 to 88% of all NPs), Al (27 to 37%), Ti (7 to 22%), Mn (8 to 15%), Ba (6 to 12%), and Pb (2 to 9%) were the most abundant particles detected by SP-ICP-TOF-MS. All other detected particles represented <6% of the total number of detected particles (Fig. 3a). A consistent conclusion was obtained by elemental ratio analysis in section 3.2. Nanoparticles occurred as either smNPs (Fig. 3b) or mmNPs (Fig. 3c). For each element, smNPs accounted for <50% of the total number of detected elements (Fig. S4d†). The majority of the detected elements occurred as mmNPs (Fig. S4e†). The mmNPs were further classified into clusters of particles with similar elemental compositions (Fig. S5†). The intra-sample clustering revealed that dust samples contained various classes/groups of mmNPs including Al, Fe, Ti, Mn, Ba, Sr, Zr, Ce, Y, Th, Cr, Ni, Zn, Cu, Sn, Sb, Pb, and W-rich mmNPs (Fig. S5a,† 4). The inter-sample clustering revealed that some mmNPs are conserved across all dust samples and others are present in a few dust samples (Fig. S5b,† 4). For instance, AlFeTi, FeAlTi, TiFeMn, CeLaNd, ZrYTh, MnBaPb, CePbMn, SrBaCe, and ThUDy were identified in all dust samples; MnBaPb, SnPbSb, ZnMnSn, and CuSnPb were identified in six dust samples; PbBaSn and YThDy were identified in five dust samples; BaPbSe and SbPbCu were identified in four dust samples; TiAlFe and NiSbCr were identified in three dust samples; and ZnCuSn was identified in only one dust sample (Fig. S5b,† 4). Six clusters of Al, Fe, Ti, Ce, Zr, and Mn-rich particles accounted for the large majority (>97%) of mmNPs across all samples (Fig. 4). Other

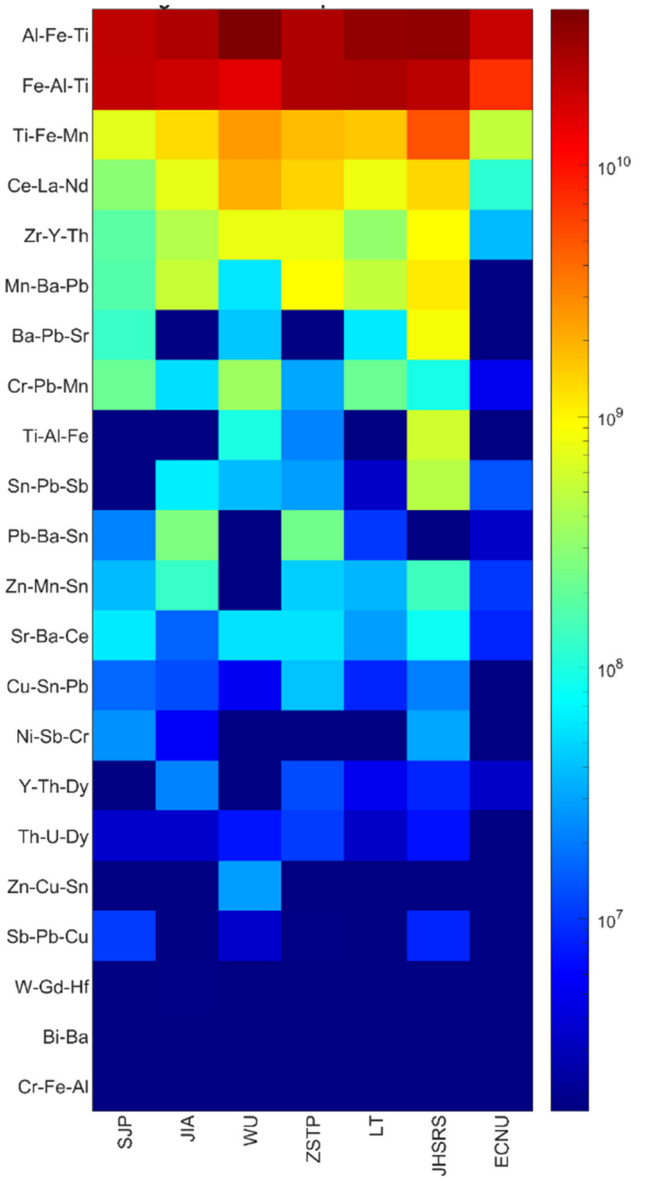

Fig. 4 Heat maps of the number concentration (particles per g) of mmNPs in all dust samples. The first and second stage distance cutoffs were set at 0.5 and 0.1, respectively. Clusters are labeled by the three elements with the highest mass fractions in each cluster.

clusters with low numbers of mmNPs include Cr, Sn, Zn, Cu, Ni, Sb, and W-rich mmNP clusters. The mean elemental composition of the major different mmNP clusters is presented in Fig. 5 and S7.† This illustrates that AlFeTi (Ti/Al = 0.10 ± 0.02), FeAlTi (Ti/Fe = 0.23 ± 0.06), TiFeMn (Ti/Nb = 346 ± 108), CeLaNd (Ce/La = 1.95 ± 0.15), and ZrCeY (Zr/Hf = 37.4 ± 8.5) clusters are typical of natural occurring mmNPs (Fig. S6†).[17,18] Other mmNP clusters were mainly rich in Cr, Ni, Zn, Cu, Pb, Sn, and Sb with low trace concentrations of other elements (Fig. 5). They are attributed to anthropogenic contamination, most likely brake wear and/or tire emissions,[30–32] which is consistent with the result of elemental analysis in section 3.1. Similar results are also observed in urban runoff.[18,37,38] Below, we discuss all particles containing Cr, Ni, Zn, Pb, Sn, and Sb in more detail.

Pb, Zn, Cr, and Ni-bearing NPs. Pb-, Zn-, Cr-, and Ni-bearing particles represented 2.1 to 9.3%, 0.8 to 4.6%, 0.9 to 6.1%, and 0.2 to 1.0% of all detected particles. These elements were dominantly (>72%) associated with Fe-containing particles. The mass elemental ratios of Pb/Fe, Zn/Fe, Ni/Fe, and Cr/Fe in Fe-bearing particles are presented in Fig. 6 and illustrate that the majority of these elements occur as a minor phase in iron-rich particles. Pb/Fe, Zn/Fe, and Ni/Fe each exhibit similar ratios in all dust samples suggesting that each of these particle types might originate from the same source. These elemental ratios are most likely typical of naturally occurring particles. The average elemental ratios of Pb/Fe, Zn/Fe, and Ni/Fe determined at the single particle level in soil natural particles are 0.014 ± 0.066, 0.36 ± 0.54, and 0.022 ± 0.033.[17,18] Additionally, some particles displayed Pb/Fe, Zn/Fe, and Ni/Fe > 1.0, which correspond to the particles identified in the Pb, Zn, and Ni rich clusters (Fig. 5). Cr/Fe exhibits a broader distribution, as well as a higher fraction with mmNPs with Cr/Fe > 1.0, in the SJP dust (near a large-scale sand mining ship factory) compared to all the other dust samples. The majority of Cr- and Fe-bearing particles in the JIA, WU, ZSTP, and JHSRS samples exhibit a Cr/Fe ratio of < 0.1, most likely typical of naturally occurring Cr- and Fe-bearing particles (natural Cr/Fe determined at the single particle level = 0.08 ± 0.15).[17] In contrast the SJP, LT, and ECNU dust samples contain Cr- and Fe- with higher elemental ratios and in particular the SJP dust contains Cr

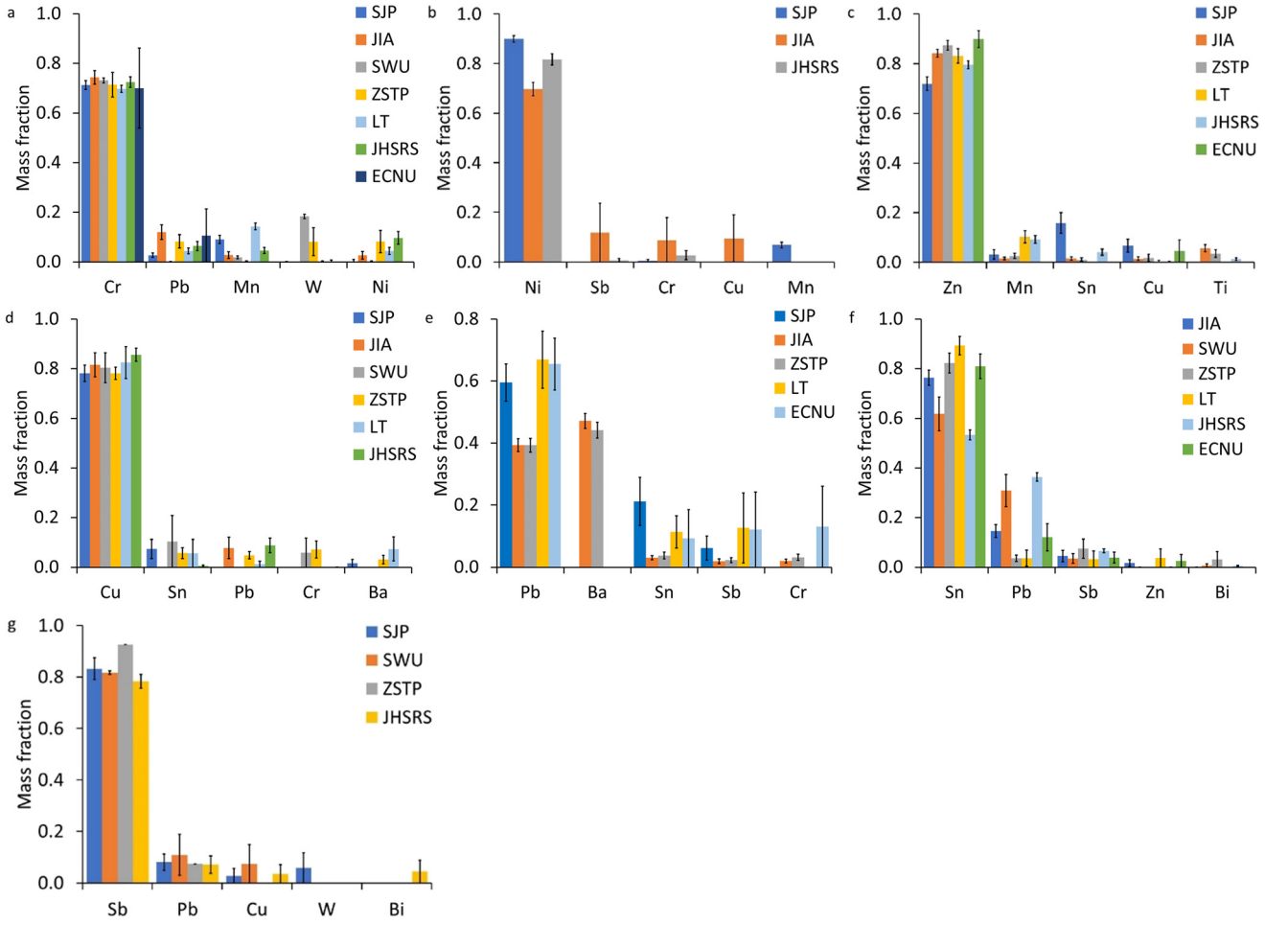

Fig. 5 Mean elemental mass composition of anthropogenic mmNP clusters identified in the dust samples (a) Cr-, (b) Ni-, (c) Zn-, (d) Cu-, (e) Pb-, (f) Sn-, and (g) Sb-bearing particles.

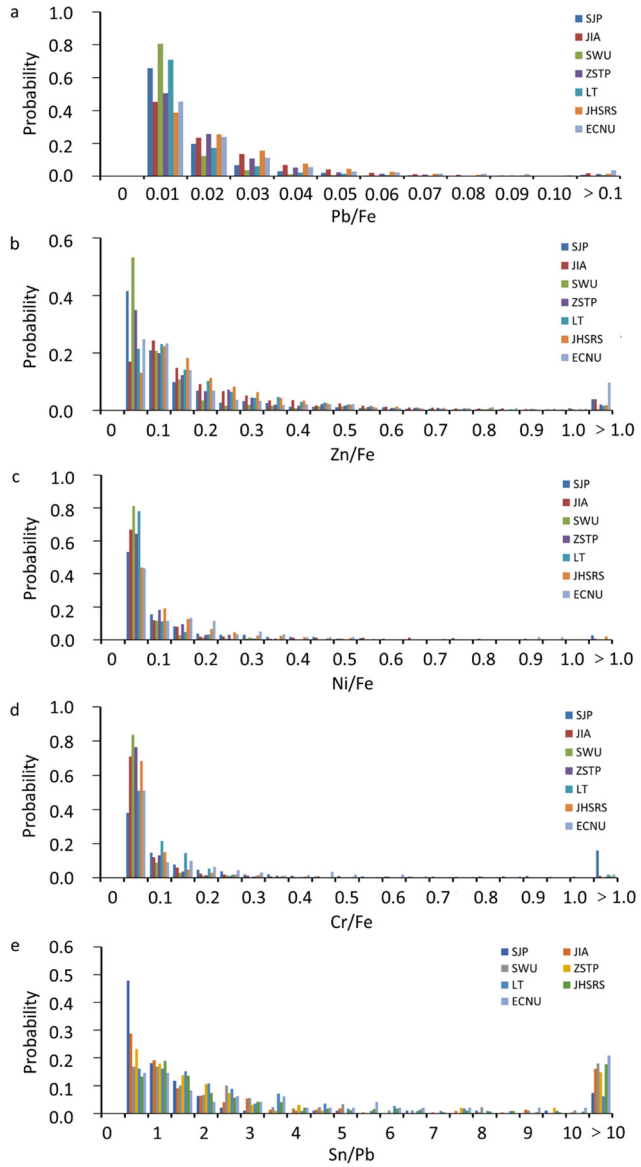

Fig. 6 Mass elemental ratios of (a) Pb/Fe, (b) Zn/Fe, (c) Ni/Fe, and (d) Cr/Fe, and (e) molar elemental ratio of Sn/Pb.

and Fe containing particles with a Cr/Fe elemental mass ratio of up to 3, most likely anthropogenic particles such as $FeCr_2O_4$ (Cr/Fe mass ratio = 1.86). This is consistent with the high concentrations of Cr and Fe in the SJP dust as well as the identification of $FeCr_2O_4$ in the SJP dust by TEM analysis. Additionally, the SJP dust contained a high proportion of Cr-dominantly containing particles compared to the other dust samples (Fig. 6d).

Sn-bearing NPs. Sn-bearing particles represented 0.3 to 1.8% of all detected particles (Fig. S4†). Sn-bearing particles were either smNPs (28–44%) or mmNPs (56–72%). Within the mmNPs, Sn occurred as a major phase in the SnPbFe cluster, or as a trace element in the other clusters, dominantly FeAlSn (65–91% of all Sn mmNPs) and AlFeSn (0–27% of Sn mmNPs) clusters (Fig. 7a). Sn also occurred in association with many other elements such as Cr, Mn, Ni, Cu, Zn, Zr, Sb, Pb, *etc.* The elemental ratio of Sn/Pb in Sn and Pb-bearing NPs varied between 0.02 and 500 with most particles (>60%) exhibiting Sn/Pb < 4.0 (Fig. 6e). These elemental associations suggest the anthropogenic nature of Sn, which is widely used in the electroplating industry, and most likely released from the non-exhaust emission of vehicles as all these elements are used in brake pads and other vehicle component materials.[18,30,31]

W-containing NPs. Few W-containing NPs, accounting for 0.1–0.6 of all detected NPs, were also identified in all samples as smNPs (28–63% of all W-bearing NPs) and mmNPs (37–72% of all W-bearing NPs) (Fig. 3). Within mmNPs, W occurred mostly as a minor element in other metal rich particles such as Fe, Cr, Ti, and Al (Fig. 7b). The identification of W-containing particles (both as smNPs and mmNPs) and the higher bulk W/Al elemental ratios than the natural reference elemental ratios (Fig. S2e†) suggest the anthropogenic nature of W in the dust samples. W occurred in association with many other elements such as Mn, Ni, Cu, Zn, Zr, Sn, Sb, Pb, *etc.* These elemental associations suggest the anthropogenic nature of W most likely from brake wear emissions as all these elements are used in the brake pad material.[18,32,33]

3.4. Microscopy analysis

Due to the elevated metals in the SJP dust and JHSRS dust samples, these two samples were selected for the electron microscopy analysis, and numerous Ti-, Fe-, Zn-, Ce-La-, Zr-, Pb-, and Sn-containing NPs were identified in these two dust samples. W-rich particles were observed by SEM in the JHSRS dust. In addition, Ti-containing NPs were observed more frequently in the JHSRS dust (around 83% of Ti-containing NPs were identified in JHSRS dust), and Fe-containing NPs were more frequently observed in the SJP dust (around 80% of Fe-containing NPs were identified in the SJP dust), which was consistent with the results of total elemental concentration analysis that Ti and Fe were most abundant in the JHSRS dust and SJP dust, respectively. The following describes specifically what was found/determined directly with electron microscopy.

Titanium oxides. Titanium oxides, including rutile, anatase and Magnéli (Ti_xO_{2x-1}) phases, with different sizes ranging from 60 to 400 nm, are ubiquitous in the Shanghai dust samples (Fig. 8a and c and S7†). The observed *d*-spacings of 2.01 Å and 2.42 Å in the different crystals matched with the (1 0 4) lattice plane of rutile and (1 0 3) lattice plane of anatase, respectively. A typical Ti_xO_{2x-1} phase in the size range of 200–250 nm was identified with observed *d*-spacings of 3.36 and 3.08, corresponding to the (−1 2 0) and (0 0 4) lattice planes of Ti_4O_7 (Fig. 8a). STEM showed that these titanium oxides were often associated with minor amounts of Ca, Fe, Si, Al, Na and Zn. Titanium oxides are common engineered particles and widely used in sunscreens, paints and photocatalysts. Moreover, according to the study by Yang *et al.*,[11] Ti_xO_{2x-1} is a tracer for tracking solid-state

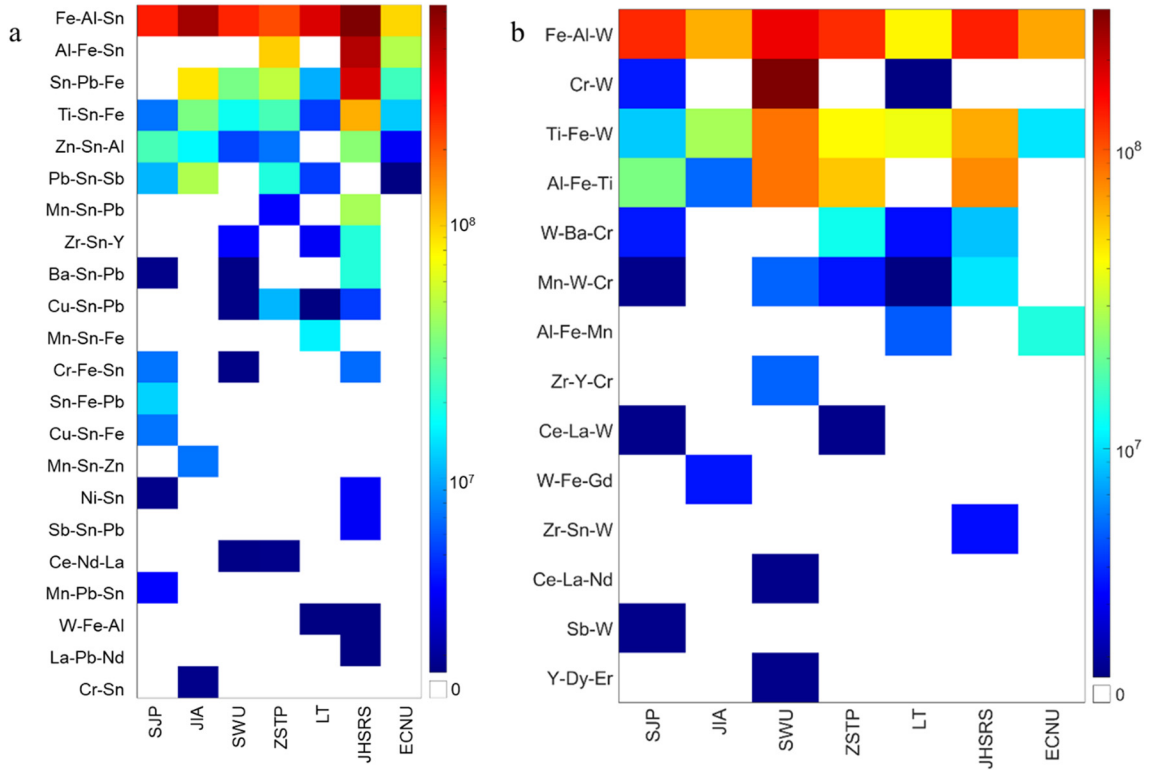

Fig. 7 Reclustering of (a) Sn-bearing mmNPs and (b) W-bearing mmNPs.

emissions worldwide from industrial coal-burning, suggesting the occurrence of anthropogenic Ti oxide particles in the road dust samples.

Iron-containing particles. Various Fe-containing NPs (<100 nm) and ultrafine particles (<1000 nm), including ilmenite ($FeTiO_3$), hematite (Fe_2O_3), magnetite (Fe_3O_4), pyrrhotite ($Fe_{(1-x)}S$), fayalite (Fe_2SiO_4) and Fe–Cr oxides ($FeCr_2O_4$), were found in the SJP dust, and only magnetite was identified in the JHSRS dust. For example, as shown in Fig. S8a,† a polygonal monocrystalline ilmenite particle in the size range of 300–400 nm was identified with observed *d*-spacings of 3.65 Å, corresponding to the (0 1 2) lattice plane of ilmenite. EDS indicated that Si, Mg and small amounts of Mn were also present. Further, hematite, magnetite and fayalite particles, with a size range of several nanometers to 400 nm, are ubiquitous in the dust samples. For example, as shown in Fig. S8b,† around 300 nm hematite was identified with *d*-spacings of 3.62, 2.27 and 2.14 Å, which agreed with the (0 1 2), (0 0 6) and (1 1 3) lattice spacings, respectively, for hematite. 200–300 nm magnetite was also identified with *d*-spacings of 2.15, 1.66 and 1.42 Å (Fig. S8d†), which matched with the (1 2 2), (0 4 4) and (1 3 5) lattice planes of magnetite. An example of the aggregation of monocrystalline and polycrystalline fayalite NPs in the size of several nanometers and 100–200 nm, respectively, is shown in Fig. S8e† with the identifying characteristic *d*-spacings of 4.37, 3.69, 3.51 and 2.46 Å, corresponding to the (1 1 0), (1 0 1), (1 1 1) and (1 1 2) lattice spacings, respectively, for fayalite. As shown in Fig. S8c,† a pyrrhotite aggregate with a crystal size of 50–400 nm was also identified with *d*-spacings of 5.31 and 2.15 Å, which matched with its (2 0–2) and (1 3 3) lattice planes, respectively. A polycrystalline Fe–Cr oxide in the primary size of several nanometers was also identified with a characteristic *d*-spacing of 3.45 Å (Fig. S8f†), which matched with the (2 0 2) lattice plane of $FeCr_2O_4$. According to the STEM results, these Fe-containing NPs were often associated with minor amounts of Ca, Al, Si, K, Mg, Mn, Cr and Zn. Ilmenite and fayalite are common natural forms of Fe-containing particles. Besides the natural source, magnetic particles (including magnetite and hematite) in road dust can also be derived from coal fly ash (usually spherical)[39] and vehicle emissions by abrasion of engine or vehicle body materials, which are typically non-spherical.[7] The non-spherical magnetic particles (Fig. S8b and S8d†) could be related to the vehicle emission. Moreover, the elemental and crystallographic analyses by electron microscopy support the observation obtained by the other methods. For instance, Fig. S8a† shows that ilmenite Ti–Fe-containing particles observed by transmission electron microscopy are in good agreement with the Ti/Fe elemental ratios obtained by SP-ICP-TOF-MS (Fig. S3b†).

W-containing particles. Numerous W-containing particles in the size range of 50–700 nm were found by SEM in the dust sample from the Jinshan high speed rail station (Fig. 8b). According to the EDS results, these particles were frequently associated with minor amounts of Ti and Fe. The abundance of W-containing particles in dust samples collected near a high-speed rail station supports the total

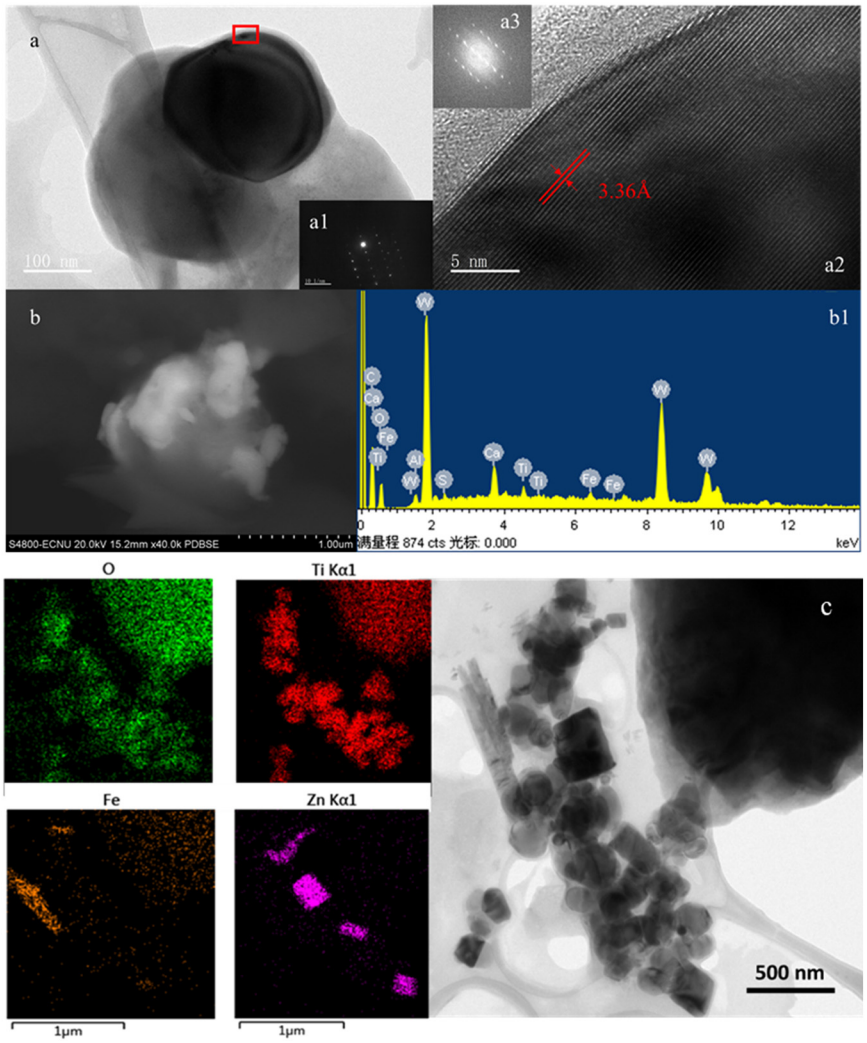

Fig. 8 Typical electron microscopy micrographs of Ti-containing NPs (a: Ti_4O_7) and W-containing particles (b) in dust samples, where a1 and a2 are the corresponding SAED image and the magnification of selected area of a, a3 is the FFT image of a2, and b1 is the EDS of b. (c) STEM images of Ti, Fe, and Zn oxide nanoparticles in the dust samples.

elemental concentration and ratio data, suggesting W contamination in the road dust sample (Fig. S2e†). As mentioned above, these W-containing NPs could be derived from the friction of brake pads and other vehicular components.[32,33,40]

Other nanoparticles. Pb–Sn-, Ce–La-, Zn- and Zr-containing NPs were also commonly found in the Shanghai dust samples (Fig. S9–S12†). Ubiquitous $Pb_2Sn_2O_6$ nanoparticles in the size range from several nanometers to 50 nm were observed by SEM and TEM (Fig. S9†). These NPs were identified with the characteristic *d*-spacings of 5.32, 3.23, 2.98 and 2.63 Å, corresponding to the (2 0 0), (1 1 3), (2 3 0) and (2 2 3) lattice spacings of $Pb_2Sn_2O_6$, respectively, and found to be associated with trace amounts of Fe and Au by EDS. These elemental associations are consistent with those detected by SP-ICP-TOF-MS (Fig. 5f). This is also consistent with the molar Sn/Pb elemental ratio calculated at the single particle level, where the majority of the particles display a Sn/Pb < 4 (Fig. 6e). Ce–La-containing NPs in the size range from several nanometers to 150 nm were identified with the characteristic *d*-spacings of 4.38, 3.38, 2.99 and 2.24 Å, corresponding to the (0 1 1), (1 1 0), (2 0 0) and (1 2 0) lattice spacings, respectively, for stillwellite-(Ce) (Fig. S10†). According to the EDS results, minor amounts of Nd, Th and Au were often found to be associated with these Ce–La-rich particles. These observations are consistent with the elemental composition of the Ce-rich particle cluster identified by SP-ICP-TOF-MS (Fig. S6d†), which is typical of naturally occurring NPs.[17] Zn-containing particles, including zincite and smithsonite, were found in both dust samples in the size range of 50–500 nm (Fig. S11†), and identified with the characteristic *d*-spacings of 2.52 Å and 2.72 Å, in agreement with the (1 0 1) lattice spacing of zincite and (1 0 4) lattice spacing of smithsonite, respectively. Zr-containing particles, including Zr–Sc phosphate and baddeleyite, were found in both dust samples in the size range of 100–200 nm (Fig. S12†), and identified with the characteristic *d*-spacings of 4.32 Å and 2.91 Å, in agreement with the (1 0 1) lattice

spacing of pretulite and (1 1 1) lattice spacing of baddeleyite, respectively. According to the EDS results, minor amounts of Y and Fe were often associated with these Zr-rich particles. These observations are consistent with the elemental composition of the Zr-rich particle cluster identified by SP-ICP-TOF-MS (Fig. S6e†), which is typical of naturally occurring NPs.[17] These naturally occurring particles, such as stillwellite-(Ce) and pretulite, and incidental particles, such as Pb–Sn containing particles, were in good agreement with the results of PCA analysis. For instance, the co-existence of Pb and Sn indicated a Pb–Sn alloy source which has been widely used in the electroplating industry.

4. Conclusions

In the present study, a comprehensive analytical approach was used for the characterization, quantification and discrimination of natural and anthropogenic metal-containing particles from Shanghai road dust. In addition to the total elemental concentration and elemental ratio analysis based on the bulk dust samples, the multi-element single particle analysis of Shanghai road dust was achieved using SP-ICP-TOF-MS, and typical NPs were further identified based on TEM coupled with EDS and SAED techniques. The natural source of Ti and the anthropogenic source of W in the dust samples were discriminated by PCA analysis on the total elemental concentrations. The anthropogenic sources of W, Ti, Pb, and Sn were further indicated by correlation analysis and bulk element ratio analysis. The lower bound of anthropogenic Ti, W, Pb, and Pb concentrations was estimated to be 0.25–1.48 × 10^6 μg kg^{-1}, 0.19–1.21 × 10^5 μg kg^{-1}, 0.98–4.22 × 10^4 μg kg^{-1}, and 0.12–1.01 × 10^4 μg kg^{-1}, respectively. The number concentrations of Ti, W, Pb, and Sn-containing NPs in the Shanghai road dust samples were determined by SP-ICP-TOF-MS and they varied in the range of 0.66–3.3 × 10^{10} particles per g for Ti-containing NPs, 0.23–1.51 × 10^{10} particles per g for Pb-containing NPs, 0.28–3.10 × 10^9 particles per g for Sn-containing NPs, and 1.34–9.38 × 10^8 particles per g for W-containing NPs. Many clusters, such as MnBaPb, SnPbSb, ZnMnSn, and CuSnPb, were found to be rich in Cr, Ni, Zn, Cu, Pb, Sn, Sb, and W, which could be attributed to anthropogenic contamination. Moreover, numerous Ti-, Pb-, Sn- and W-rich particles, which could originate from the non-exhaust emission of vehicles, were identified in the Shanghai road dust samples by TEM. Besides natural TiO_2 NPs, such as rutile and ilmenite, the typical Magnéli phase of TiO_2 NPs was also found in Shanghai road dust, which could be a tracer for tracking solid-state emissions worldwide from industrial coal-burning and be considered as evidence of anthropogenic contamination of Ti-containing NPs. The analyses for the other metal-containing NPs based on this comprehensive analytical approach are also consistent. For instance, the co-existence of Pb–Sn and Zr–Y in mmNPs was illustrated by EDS (Fig. S9 and S13†), SP-ICP-TOF-MS (Fig. S5†), and PCA analysis. Overall, this study provides a reliable comprehensive approach for the characterization of road dust particles and gives new insights into the nature of Ti-, Pb-, Sn- and W-bearing particles in dust samples.

Conflicts of interest

The authors declare that they have no competing interests.

Acknowledgements

This study was supported by the National Natural Science Foundation of China (42125102) and the United States National Science Foundation (Grants No. 1553909 and 1828055). Additional funding for this work was provided by the Fundamental Research Funds for the Central Universities and the Open Foundation of East China Normal University (ECNU).

References

1 J. Lelieveld, J. S. Evans, M. Fnais, D. Giannadaki and A. Pozzer, The contribution of outdoor air pollution sources to premature mortality on a global scale, *Nature*, 2015, **525**, 367.
2 R. A. Rohde and R. A. Muller, Air Pollution in China: Mapping of Concentrations and Sources, *PLoS One*, 2015, **10**, e0135749.
3 HEI, *State of Global Air 2020*, Health Effects Institute, Boston, MA, 2020.
4 B. A. Maher, I. A. M. Ahmed, V. Karloukovski, D. A. MacLaren, P. G. Foulds, D. Allsop, D. M. A. Mann, R. Torres-Jardon and L. Calderon-Garciduenas, Magnetite pollution nanoparticles in the human brain, *Proc. Natl. Acad. Sci. U. S. A.*, 2016, **113**, 10797–10801.
5 M. R. Miller, J. B. Raftis, J. P. Langrish, S. G. McLean, P. Samutrtai, S. P. Connell, S. Wilson, A. T. Vesey, P. H. B. Fokkens, A. J. F. Boere, P. Krystek, C. J. Campbell, P. W. F. Hadoke, K. Donaldson, F. R. Cassee, D. E. Newby, R. Duffin and N. L. Mills, Inhaled Nanoparticles Accumulate at Sites of Vascular Disease, *ACS Nano*, 2017, **11**, 4542–4552.
6 B. A. Maher, Airborne Magnetite- and Iron-Rich Pollution Nanoparticles: Potential Neurotoxicants and Environmental Risk Factors for Neurodegenerative Disease, Including Alzheimer's Disease, *J. Alzheimer's Dis.*, 2019, **71**, 361–375.
7 Y. Yang, M. Vance, F. Tou, A. Tiwari, M. Liu and M. F. Hochella, Jr., Nanoparticles in road dust from impervious urban surfaces: distribution, identification, and environmental implications, *Environ. Sci.: Nano*, 2016, **3**, 534–544.
8 R. K. Khan and M. A. Strand, Road dust and its effect on human health: a literature review, *Epidemiol. Health*, 2018, **40**, e2018013.
9 S. Chen, X. Zhang, J. Lin, J. Huang, D. Zhao, T. Yuan, K. Huang, Y. Luo, Z. Jia, Z. Zang, Y. A. Qiu and L. Xie, Fugitive Road Dust PM2.5 Emissions and Their Potential Health Impacts, *Environ. Sci. Technol.*, 2019, **53**, 8455–8465.

10 D. Salameh, J. Pey, C. Bozzetti, I. El Haddad, A. Detournay, A. Sylvestre, F. Canonaco, A. Armengaud, D. Piga, D. Robin, A. S. H. Prevot, J. L. Jaffrezo, H. Wortham and N. Marchand, Sources of PM2.5 at an urban-industrial Mediterranean city, Marseille (France): Application of the ME-2 solver to inorganic and organic markers, *Atmos. Res.*, 2018, **214**, 263–274.

11 Y. Yang, B. Chen, J. Hower, M. Schindler, C. Winkler, J. Brandt, R. Di Giulio, J. Ge, M. Liu, Y. Fu, L. Zhang, Y. Chen, S. Priya and M. F. Hochella, Jr., Discovery and ramifications of incidental Magneli phase generation and release from industrial coal-burning, *Nat. Commun.*, 2017, **8**, 194.

12 F. Tou, Y. Yang, J. Feng, Z. Niu, H. Pan, Y. Qin, X. Guo, X. Meng, M. Liu and M. F. Hochella, Environmental Risk Implications of Metals in Sludges from Waste Water Treatment Plants: The Discovery of Vast Stores of Metal Containing Nanoparticles, *Environ. Sci. Technol.*, 2017, **51**, 4831–4840.

13 A. Praetorius, A. Gundlach-Graham, E. Goldberg, W. Fabienke, J. Navratilova, A. Gondikas, R. Kaegi, D. Günther, T. Hofmann and F. von der Kammer, Single-particle multi-element fingerprinting (spMEF) using inductively-coupled plasma time-of-flight mass spectrometry (ICP-TOFMS) to identify engineered nanoparticles against the elevated natural background in soils, *Environ. Sci.: Nano*, 2017, **4**, 307–314.

14 A. Gondikas, F. von der Kammer, R. Kaegi, O. Borovinskaya, E. Neubauer, J. Navratilova, A. Praetorius, G. Cornelis and T. Hofmann, Where is the nano? Analytical approaches for the detection and quantification of TiO2 engineered nanoparticles in surface waters, *Environ. Sci.: Nano*, 2018, **5**, 313–326.

15 K. Mehrabi, D. Gunther and A. Gundlach-Graham, Single-particle ICP-TOFMS with online microdroplet calibration for the simultaneous quantification of diverse nanoparticles in complex matrices, *Environ. Sci.: Nano*, 2019, **6**, 3349–3358.

16 S. Naasz, S. Weigel, O. Borovinskaya, A. Serva, C. Cascio, A. K. Undas, F. C. Simeone, H. J. P. Marvin and R. J. B. Peters, Multi-element analysis of single nanoparticles by ICP-MS using quadrupole and time-of-flight technologies, *J. Anal. At. Spectrom.*, 2018, **33**, 835–845.

17 M. Baalousha, J. Wang, M. Erfani and E. Goharian, Elemental fingerprints in natural nanomaterials determined using SP-ICP-TOF-MS and clustering analysis, *Sci. Total Environ.*, 2021, **792**, 148426.

18 J. Wang, M. M. Nabi, M. Erfani, E. Goharian and M. Baalousha, Identification and quantification of anthropogenic nanomaterials in urban rain and runoff using single particle-inductively coupled plasma-time of flight-mass spectrometry, *Environ. Sci.: Nano*, 2022, **9**, 714–729.

19 M. M. Nabi, J. Wang and M. Baalousha, Episodic surges in titanium dioxide engineered particle concentrations in surface waters following rainfall events, *Chemosphere*, 2021, **263**, 128261.

20 M. M. Nabi, J. Wang, E. Goharian and M. Baalousha, Temporal variation in TiO2 engineered particle concentrations in the Broad River during dry and wet weathers, *Sci. Total Environ.*, 2022, **807**, 151081.

21 F. Loosli, Z. Yi, D. Berti and M. Baalousha, Toward a better extraction of titanium dioxide engineered nanomaterials from complex environmental matrices, *NanoImpact*, 2018, **11**, 119–127.

22 Z. Tang, L. Wu, Y. Luo and P. Christie, Size fractionation and characterization of nanocolloidal particles in soils, *Environ. Geochem. Health*, 2009, **31**, 1–10.

23 L. Hendriks, A. Gundlach-Graham, B. Hattendorf and D. Guenther, Characterization of a new ICP-TOFMS instrument with continuous and discrete introduction of solutions, *J. Anal. At. Spectrom.*, 2017, **32**, 548–561.

24 H. E. Pace, N. J. Rogers, C. Jarolimek, V. A. Coleman, C. P. Higgins and J. F. Ranville, Determining Transport Efficiency for the Purpose of Counting and Sizing Nanoparticles via Single Particle Inductively Coupled Plasma Mass Spectrometry, *Anal. Chem.*, 2011, **83**, 9361–9369.

25 M. Tanner, Shorter signals for improved signal to noise ratio, the influence of Poisson distribution, *J. Anal. At. Spectrom.*, 2010, **25**, 405–407.

26 K. Mehrabi, R. Kaegi, D. Gunther and A. Gundlach-Graham, Emerging investigator series: automated single-nanoparticle quantification and classification: a holistic study of particles into and out of wastewater treatment plants in Switzerland, *Environ. Sci.: Nano*, 2021, **8**, 1211–1225.

27 M. M. Maricq, Chemical characterization of particulate emissions from diesel engines: A review, *J. Aerosol Sci.*, 2007, **38**, 1079–1118.

28 H. M. Prichard and P. C. Fisher, Identification of Platinum and Palladium Particles Emitted from Vehicles and Dispersed into the Surface Environment, *Environ. Sci. Technol.*, 2012, **46**, 3149–3154.

29 Y. F. Wang, K. L. Huang, C. T. Li, H. H. Mi, J. H. Luo and P. J. Tsai, Emissions of fuel metals content from a diesel vehicle engine, *Atmos. Environ.*, 2003, **37**, 4637–4643.

30 F. P. Kukutschová Jana, Review of Brake Wear Emissions: A Review of Brake Emission Measurement Studies: Identification of Gaps and Future Needs, *Non-Exhaust Emiss.*, 2018, 123–146.

31 A. Thorpe and R. M. Harrison, Sources and properties of non-exhaust particulate matter from road traffic: A review, *Sci. Total Environ.*, 2008, **400**, 270–282.

32 C. T. Foo, B. Omar and A. S. Jalil, A review on recent wheel/rail interface friction management, *J. Phys.: Conf. Ser.*, 2018, **1049**, 012009.

33 A. Furberg, R. Arvidsson and S. Molander, Dissipation of tungsten and environmental release of nanoparticles from tire studs: A Swedish case study, *J. Cleaner Prod.*, 2019, **207**, 920–928.

34 T. Zack, A. Kronz, S. F. Foley and T. Rivers, Trace element abundances in rutiles from eclogites and associated garnet mica schists, *Chem. Geol.*, 2002, **184**, 97–122.

35 D. P. Macwan, P. N. Dave and S. Chaturvedi, A review on nano-TiO2 sol-gel type syntheses and its applications, *J. Mater. Sci.*, 2011, **46**, 3669–3686.

36 M. T. Noman, M. A. Ashraf and A. Ali, Synthesis and applications of nano-TiO2: a review, *Environ. Sci. Pollut. Res.*, 2019, **26**, 3262–3291.
37 E. R. McKenzie, J. E. Money, P. G. Green and T. M. Young, Metals associated with stormwater-relevant brake and tire samples, *Sci. Total Environ.*, 2009, **407**, 5855–5860.
38 M. Legret and C. Pagotto, Evaluation of pollutant loadings in the runoff waters from a major rural highway, *Sci. Total Environ.*, 1999, **235**, 143–150.
39 J. Wu, F. Tou, Y. Yang, C. Liu, J. C. Hower, M. Baalousha, G. Wang, M. Liu and M. F. Hochella, Jr., Metal-Containing Nanoparticles in Low-Rank Coal-Derived Fly Ash from China: Characterization and Implications toward Human Lung Toxicity, *Environ. Sci. Technol.*, 2021, **55**, 6644–6654.
40 D. M. Chapman, Behavior of titania-supported vanadia and tungsta SCR catalysts at high temperatures in reactant streams: Tungsten and vanadium oxide and hydroxide vapor pressure reduction by surficial stabilization, *Appl. Catal., A*, 2011, **392**, 143–150.